


Topological nature of non-Hermitian degenerate bands in structural parameter space

Olivia Y. Long^{1,*}, Cheng Guo,¹ and Shanhui Fan^{1,2,†}

¹*Department of Applied Physics, Stanford University, Stanford, California 94305, USA*

²*Ginzton Laboratory and Department of Electrical Engineering, Stanford University, Stanford, California 94305, USA*

 (Received 27 May 2023; revised 9 November 2023; accepted 15 November 2023; published 30 November 2023)

In photonics, band degeneracies at high-symmetry points in wavevector space have been shown to exhibit rich physical phenomena. However, obtaining degenerate bands away from such points is highly nontrivial. In this work, we achieve complex band degeneracy in a photonic crystal structure over a region of momentum space. We show that this band degeneracy corresponds to polarization-independent transmission, which can be harnessed for nonlocal metasurface design. Moreover, we find that the band degeneracy manifests as a topological singularity in the structural parameter space of the system. Our work highlights the importance of topological concepts in the design of polarization-independent photonic structures.

DOI: [10.1103/PhysRevApplied.20.L051001](https://doi.org/10.1103/PhysRevApplied.20.L051001)

In the development of energy band theory for Hermitian systems, band degeneracies at isolated points in momentum space have played a significant role. Well-known examples of such band degeneracies include the Dirac [1] and Weyl points [2]. In photonics, such degeneracies have been used to realize rich physical phenomena, including zero-refractive-index metamaterials [3–5], frozen light at degenerate band edges [6,7], and topological phase transitions [2,8]. Moreover, these degeneracies in Hermitian band theory provide the starting point for exploring notable features such as exceptional rings and contours that are formed when non-Hermitian perturbation is introduced [9,10].

In contrast to band degeneracies at isolated points, the possibilities for achieving band degeneracy over a *region* of momentum space have received less attention in photonics. Below, for conciseness, we refer to such band degeneracies over a region as *degenerate bands*. In electronic systems, such degenerate bands occur either for systems without spin-orbit coupling, or for systems with parity-time symmetry due to the Kramers degeneracy [11]. For photonic systems, generically, spin-orbit coupling is always present and there is no Kramers degeneracy. Thus, creating degenerate bands in photonics is nontrivial. Typical point-group symmetry can create degeneracy only at isolated high-symmetry zero-dimensional points in the

Brillouin zone. Glide symmetry may result in degenerate bands, but only along high-symmetry one-dimensional lines [12,13]. In non-Hermitian band theory for two-dimensional systems, one can achieve exceptional rings, which can be considered as a form of degeneracy, but again only on a one-dimensional line of a ring [9]. The creation of degenerate bands for a two-dimensional system in a two-dimensional region of the Brillouin zone, as we will show in this paper, has not been previously achieved except for certain obvious cases such as a uniform medium.

Degenerate bands can be particularly useful in the creation of polarization-independent nonlocal metasurfaces. These metasurfaces aim to control the transmission or reflection of light as a function of in-plane wavevectors and have found applications in optical analog computing, image processing, and augmented reality systems [14–22]. Typically, these metasurfaces consist of photonic crystal slab structures, and their properties are strongly controlled by the bands of the guided resonances [23–32]. However, the properties of these guided resonances are typically polarization-dependent, which is undesirable in many applications.

Since guided resonances have radiation losses [33], their band structures are complex. Thus, to achieve complete polarization independence in the optical response of nonlocal metasurfaces, it is essential to create degenerate complex bands. Previous work on polarization-independent metasurfaces has only utilized the degeneracy of the real part of the band structure [29]. A study incorporating the entire complex band structure is still lacking.

*olong@stanford.edu

†shanhui@stanford.edu

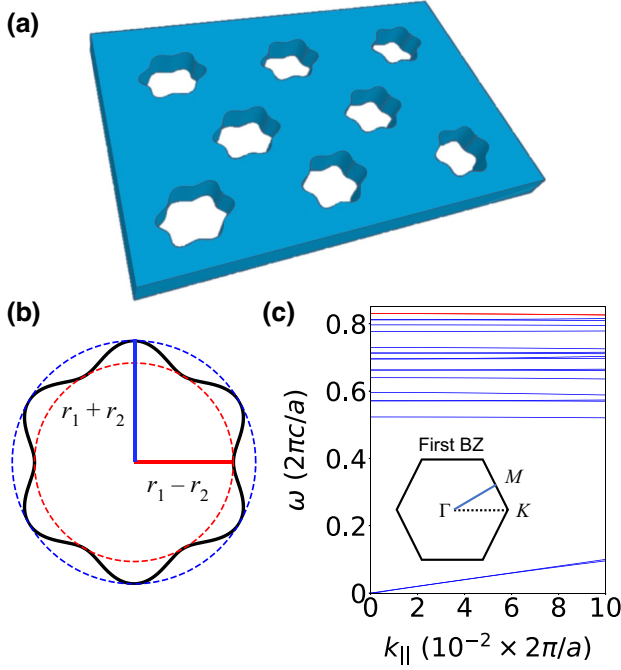


FIG. 1. (a) Photonic crystal slab with hexagonal array of air holes. The slab has lattice constant a and thickness d . The dielectric region of the crystal has relative permittivity ϵ . (b) Shape of air holes described by polar equation $r(\phi) = r_1 + r_2 \cos(6\phi)$. (c) Band structure along ΓK direction of a slab with parameters $(r_1, r_2, d, \epsilon) = (0.347a, -0.033a, 0.2475a, 13.5)$. Red lines indicate the degenerate bands under study.

In this work we show that complex degenerate bands can be achieved in nonlocal metasurfaces. Such complex degenerate bands are associated with a topological singularity in the structural parameter space of the system. We further show that this singularity can be harnessed for polarization-independent applications such as band-reject and high-pass filters, which are important in image processing and optical analog computing. Our work shows the importance of topological concepts in the design of polarization-independent nonlocal metasurfaces.

To illustrate our theory, we consider a photonic crystal slab possessing C_{6v} symmetry. Our system consists of a slab with daisy-shaped air holes arranged in a hexagonal lattice [3,34]. The slab has lattice constant a , thickness d , and the dielectric region has a relative permittivity ϵ [Fig. 1(a)]. The air holes are described by the polar equation $r(\phi) = r_1 + r_2 \cos(6\phi)$, as shown in Fig. 1(b).

For such a crystal, at normal incidence, light will only couple to a pair of doubly degenerate guided resonance bands at the Γ point due to symmetry considerations [23,35]. For this crystal with C_{6v} symmetry, the band structure is isotropic in the wavevector space near Γ , and the s and p polarizations will each couple only to a single band

[26]. In general, away from the Γ point, this pair of bands will split, yielding polarization-dependent effects.

We consider the wavevector-dependent Hamiltonian for our system derived solely from symmetry constraints. At the Γ point, the system possesses full C_{6v} symmetry. The C_{6v} group supports two different two-dimensional irreducible representations, denoted by E_1 and E_2 [13], each corresponding to a pair of doubly degenerate modes at Γ . We note that only E_1 bands can couple to normally incident light.

In the vicinity of the Γ point, we can derive an effective Hamiltonian using $\mathbf{k} \cdot \mathbf{p}$ theory. For cases where the system supports either a pair of E_1 or E_2 modes at the Γ point, the theory yields the following effective Hamiltonian [31,36]:

$$H(\mathbf{k}) = (\omega_0 - i\gamma_0)\mathbb{I} + \begin{pmatrix} u|\mathbf{k}|^2 + v(k_x^2 - k_y^2) & 2vk_x k_y \\ 2vk_x k_y & u|\mathbf{k}|^2 - v(k_x^2 - k_y^2) \end{pmatrix}, \quad (1)$$

where $u, v \in \mathbb{C}$ and ω_0, γ_0 correspond to the resonant frequency and linewidth at the Γ point, respectively. The parameters (k_x, k_y) are the components of the in-plane wavevector \mathbf{k} . The corresponding dispersion relations are

$$\omega_{\pm}(\mathbf{k}) - i\gamma_{\pm}(\mathbf{k}) = \omega_0 - i\gamma_0 + (u \pm v)|\mathbf{k}|^2, \quad (2)$$

where $+$, $-$ subscripts denote the upper and lower bands, respectively.

We can label the two bands in Eq. (2) with the polarization that each band couples to. Let $\omega_{s,p}(\mathbf{k}) = \omega_0 + C_{s,p}\mathbf{k}^2$ and $\gamma_{s,p}(\mathbf{k}) = \gamma_0 + D_{s,p}\mathbf{k}^2$, where $C_{s,p}, D_{s,p} \in \mathbb{R}$. When $C_s = C_p$ and $D_s = D_p$, we can create complex degenerate bands, which provide a polarization-independent resonant response over a range of wavevectors.

Since some of the applications of these structures concern the control of the transmission of light, we relate the differences in the complex band structure to differences in the transmission coefficients $t_{\sigma\mu}$, where μ and σ denote the polarizations of the incident and transmitted light, respectively. Only $t_{ss}(\mathbf{k})$ and $t_{pp}(\mathbf{k})$ are nonzero [26].

At an operating frequency ω , we have [23]

$$t_{\mu\mu}(\omega, \mathbf{k}) = t_d - (t_d \pm r_d) \frac{\gamma_{\mu}(\mathbf{k})}{i(\omega - \omega_{\mu}(\mathbf{k})) + \gamma_{\mu}(\mathbf{k})}, \quad (3)$$

where t_d, r_d are the direct transmission and reflection coefficients, which are assumed to be independent of frequency and wavevector. The plus or minus sign in Eq. (3) corresponds to even or odd modes with respect to the plane of the slab. Near the Γ point, we expand $t_{\mu\mu}(\omega, \mathbf{k})$ to second order with respect to k for a general ω , where $k^2 = k_x^2 + k_y^2$:

$$t_{\mu\mu}(\omega, \mathbf{k}) \approx t(\omega, \mathbf{k} = 0) - \frac{i(t_d \pm r_d)|_{\Gamma}}{(i(\omega - \omega_0) + \gamma_0)^2} \times [\gamma_0 C_{\mu} + (\omega - \omega_0)D_{\mu}] k^2. \quad (4)$$

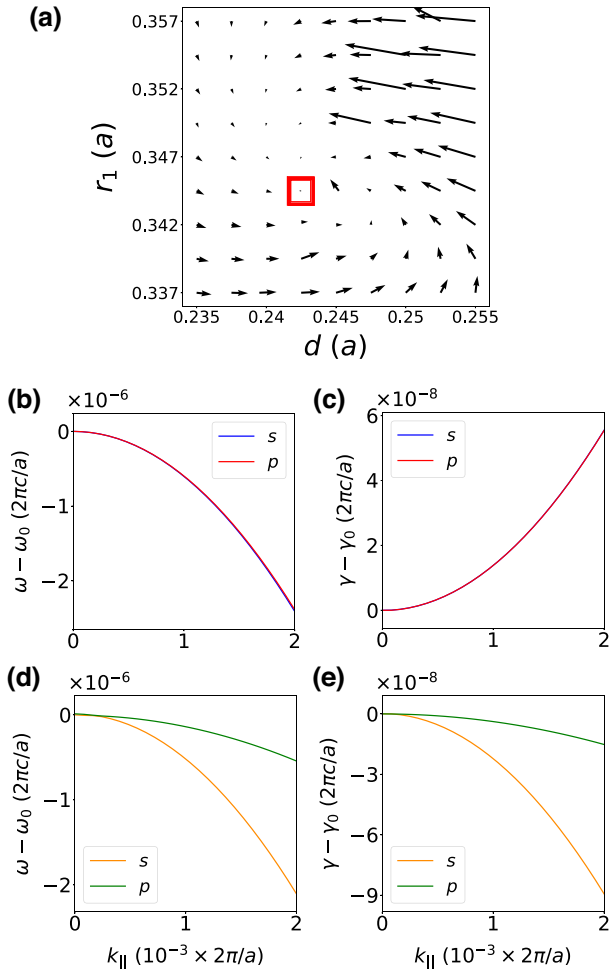


FIG. 2. (a) Vector field plot of complex \mathbf{b} vector defined in Eq. (5) showing the overall -1 topological charge around the singularity (red box). The parameters $r_2 = -0.033a$ and $\epsilon = 13.5$ are held constant, and $\omega - \omega_0 = 0.00106 \times 2\pi c/a$. (b) Band diagram of structure at topological singularity $(r_1, d) = (0.3445a, 0.2425a)$ for the real part $\omega(\mathbf{k})$ and (c) imaginary part $\gamma(\mathbf{k})$. (d) Band diagram of structure at $(r_1, r_2, d, \epsilon) = (0.33a, 0.15a, 0.34a, 13.5)$, away from the topological singularity, for the real part and (e) imaginary part.

From Eq. (4), we define a vector \mathbf{b} as a measure of how differences in C_μ and D_μ contribute to the polarization dependency $t_{ss}(\mathbf{k}) - t_{pp}(\mathbf{k})$ of the system [36]:

$$\mathbf{b} = \begin{pmatrix} \gamma_0(C_s - C_p) \\ (\omega - \omega_0)(D_s - D_p) \end{pmatrix}. \quad (5)$$

For any frequency $\omega \neq \omega_0$, $\mathbf{b} = 0$ results in $t_{ss}(\mathbf{k}) = t_{pp}(\mathbf{k})$ to the order of k^2 . When $\omega = \omega_0$, the effects of D_μ enter as higher-order k terms.

For a two-dimensional vector field in a two-dimensional parameter space, any generic isolated singularity will have an associated winding number [38]. Thus, we study the topological nature of a singularity in the \mathbf{b} field, which

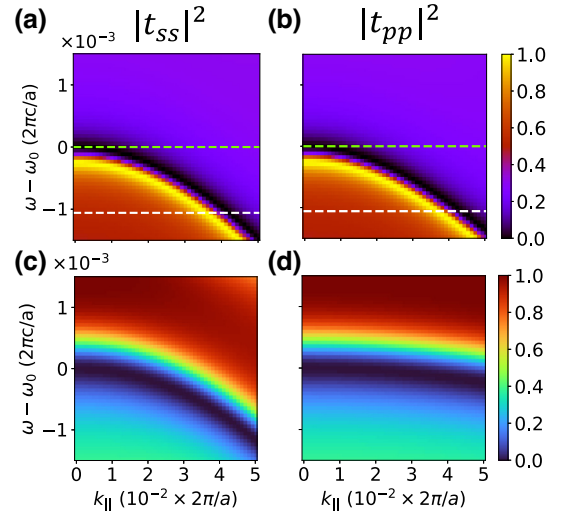


FIG. 3. (a),(b) Transmission spectra as a function of k_{\parallel} and $\omega - \omega_0$ for s and p polarizations at the topological singularity shown in Fig. 2. The dashed green and white lines indicate the operating frequencies of the high-pass and band-reject filters, respectively. (c),(d) Transmission spectra as a function of k_{\parallel} and $\omega - \omega_0$ for s and p polarizations for a structure away from the topological singularity with parameters $(r_1, r_2, d, \epsilon) = (0.33a, 0.15a, 0.34a, 13.5)$. Plots were computed using the rigorous coupled-wave analysis method [37].

corresponds to the point of complex band degeneracy, in the (r_1, d) structural parameter space. The remaining parameters are fixed: $r_2 = -0.033a$, and $\epsilon = 13.5$, which approximates Si at optical frequencies. Each point in the parameter space corresponds to a different structure. We choose to study an E_1 band near the Γ point, delineated by red bands in Fig. 1(c), which shows the band structure along the ΓK direction for the photonic crystal slab with parameters $(r_1, d) = (0.347a, 0.2475a)$. Here, the resonant frequency at the Γ point is $\omega_0 = 0.82606 \times 2\pi c/a$, where there is only zeroth-order diffraction.

As we tune (r_1, d) in our structure, we track the same E_1 mode and fit the band structures to a quadratic function to obtain C_s, C_p, D_s , and D_p . The band structures were calculated using the guided-mode expansion method [39,40]. We set $\omega - \omega_0 = 0.00106 \times 2\pi c/a$, which corresponds to the operating frequency of a filter in the wavevector domain, as discussed below. Using this value of $\omega - \omega_0$ and the linewidths γ_0 at each point in the parameter space, we employ Eq. (5) to generate the \mathbf{b} vector field shown in Fig. 2(a). The computed topological singularity is located at $(r_1, d) = (0.3445a, 0.2425a)$, where the \mathbf{b} vector magnitude is minimized [red box in Fig. 2(a)]. We see that the singularity exhibits a topological charge of -1 .

In Figs. 2(b) and 2(c), we plot the real and imaginary parts of the complex band structure at the topological singularity along the ΓK direction. Away from $\mathbf{k} = 0$, both real and imaginary parts of the frequency are indeed

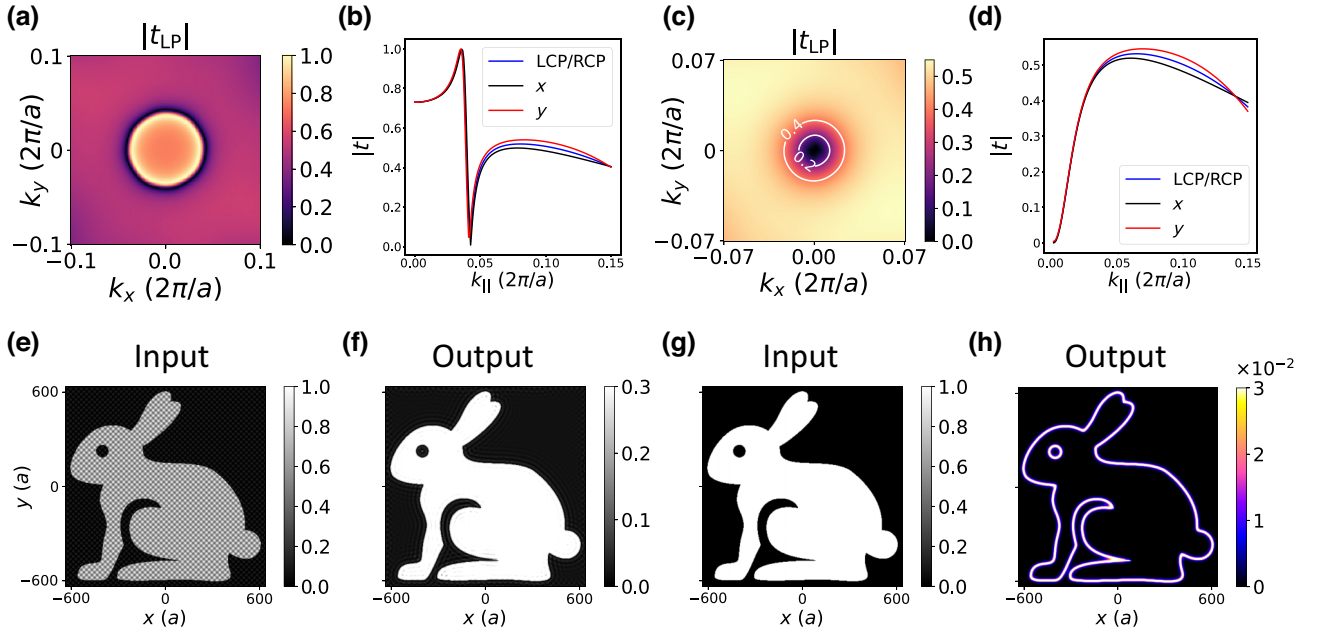


FIG. 4. Numerical demonstration of isotropic spatial frequency filters using complex band degeneracy. (a) Transfer function of band-reject filter at operating frequency $\omega = 0.8305 \times 2\pi c/a$ for 45° linearly polarized light. (b) Magnitude of band-reject filter transfer function as function of k_{\parallel} for different polarizations. (c) Transfer function at operating frequency $\omega_0 = 0.83156 \times 2\pi c/a$ for 45° linearly polarized light. (d) Magnitude of high-pass filter transfer function as function of k_{\parallel} for different polarizations. (e)–(f) Intensity profile of linearly polarized input image and transmitted output image for band-reject filter. (g)–(h) Intensity profile of linearly polarized input image and transmitted output image for high-pass filter.

degenerate. We contrast the band structure at the topological singularity with that of another photonic crystal slab structure with parameters $(r_1, r_2, d, \epsilon) = (0.33a, 0.15a, 0.34a, 13.5)$ in Figs. 2(d) and 2(e), where the dispersion relations $\omega(\mathbf{k})$ and $\gamma(\mathbf{k})$ are not degenerate away from $\mathbf{k} = 0$.

The degeneracy of the complex band structure away from the Γ point should translate to the degeneracy of the transmission coefficients in a range of wavevectors \mathbf{k} , that is, $t_{ss}(\mathbf{k}) = t_{pp}(\mathbf{k})$ for a range of \mathbf{k} . To illustrate this, Figs. 3(a) and 3(b) show the transmission of the s and p polarizations through the structure corresponding to the topological singularity. At $\mathbf{k} = 0$, the transmission spectra exhibit a minimum at the guided resonance frequency $\omega_0 = 0.83156 \times 2\pi c/a$.

Away from the Γ point, the bands continue to remain degenerate, in agreement with the band structure shown in Figs. 2(b) and 2(c). Note that the transmission spectra also exhibit similar linewidths away from the Γ point, in accordance with the degenerate imaginary band frequencies.

In contrast, the structure in Figs. 2(d) and 2(e) exhibits polarization-dependent transmission behavior, as shown in Figs. 3(c) and 3(d). The results illustrate the connection between the topological singularity and the polarization independence of the photonic slab structure over a range of frequencies and wavevectors.

We now apply the complex band degeneracy to wavevector domain filtering, which is useful for image

processing [41]. Specifically, we demonstrate isotropic high-pass and band-reject filters in wavevector space. Such filters find applications in periodic noise suppression and edge detection [41,42]. Previous photonic crystal designs for this functionality yield strong polarization dependence, which can be undesirable in practical applications [43].

To realize the band-reject filter, we choose the operating frequency to be at the frequency detuning of $\omega - \omega_0 = -0.00106 \times 2\pi c/a$, as depicted by the dashed white line in Figs. 3(a) and 3(b). The \mathbf{b} vector plot in Fig. 2 assumes the same magnitude of detuning. In Fig. 4(a), we plot the transfer function of the band-reject filter for 45° linearly polarized light, which has an s and p polarization decomposition that depends on the in-plane wavevector \mathbf{k} . Despite this \mathbf{k} -dependent mixture of polarizations, the transfer function for linearly polarized light remains isotropic and thus, polarization-independent over a wide range of k_{\parallel} , as seen in Fig. 4(b).

Although the \mathbf{b} vector is defined by a specific ω value [Eq. (5)], when $\mathbf{b} = 0$, the bands are degenerate and can thus be used to realize a high-pass filter at a different operating frequency. Specifically, we operate at the resonant frequency $\omega_0 = 0.83156 \times 2\pi c/a$, depicted by the dashed green line in Figs. 3(a) and 3(b). As in the case of the band-reject filter, the transfer function of the high-pass filter for 45° linearly polarized light is isotropic [Fig. 4(c)] and polarization-independent over a wide range of k_{\parallel} , as shown in Fig. 4(d).

Using the transfer functions for 45° linearly polarized light, we demonstrate the filter functionalities on an input image of size $1200a \times 1200a$. To generate the transmitted output images, we perform a spatial Fourier transform on the input image, multiply the Fourier transform by the transfer function, then perform the inverse Fourier transform. We utilize the wavevector range $|\mathbf{k}| = [0, 0.15] \times 2\pi/a$ to demonstrate both functionalities. For the band-reject filter, the input image is corrupted by two-dimensional periodic noise [Fig. 4(e)]. Upon transmission through the structure, the noise is eliminated in the output image, demonstrating isotropic and polarization-independent operation [Fig. 4(f)]. By changing the operating frequency, the filter can be tuned to reject any desired frequency band. To demonstrate the high-pass filter, we utilize the input image shown in Fig. 4(g). The transmitted output image shows that edges along all directions are detected, confirming the polarization independence of the device [Fig. 4(h)].

As final remarks, the f -numbers of the band-reject and high-pass filters are 2.723 and 2.726, respectively, corresponding to numerical apertures of 10.35° and 10.34° . Such specifications fall well within the range of typical camera lens apertures [44]. Thus, the optical response remains polarization-independent over a much larger range of k (about one order of magnitude larger) compared to that of the degeneracy in the band structure. This is due to the fact that the degenerate bands are well isolated from other bands, resulting in a single-resonance dominated response over a wide range of k . In addition, we note that the presence of topological charge, which guarantees $\mathbf{b} = 0$ at a singular point in the parameter space, also results in $\mathbf{b} \approx 0$ in a region in the parameter space around such a singular point. There, near such a singular point, the near polarization-independent behavior is robust against parameter variations. Higher topological charge may result in a wider parameter range where the structure has near polarization-independent behaviors.

In summary, we have shown that complex band degeneracy can be achieved over a region of wavevector space in a photonic crystal system. This degeneracy manifests as a topological singularity in the structural parameter space and can be harnessed for polarization-independent applications such as spatial frequency filters for image processing and optical analog computing. Our work highlights the importance of topological concepts in the design of polarization-independent structures.

ACKNOWLEDGMENTS

This work was supported by the Samsung Advanced Institute of Technology (SAIT) of Samsung Electronics, and by a MURI project (Grant No. FA9550-21-1-0312) from the U.S. Air Force Office of Scientific Research. O.L. acknowledges support from the NSF Graduate Research

Fellowship (Grant No. DGE-1656518) and the Stanford Graduate Fellowship.

-
- [1] F. D. M. Haldane and S. Raghu, Possible realization of directional optical waveguides in photonic crystals with broken time-reversal symmetry, *Phys. Rev. Lett.* **100**, 013904 (2008).
 - [2] L. Lu, J. D. Joannopoulos, and M. Soljačić, Topological photonics, *Nat. Photonics* **8**, 821 (2014).
 - [3] M. Minkov, I. A. D. Williamson, M. Xiao, and S. Fan, Zero-index bound states in the continuum, *Phys. Rev. Lett.* **121**, 263901 (2018).
 - [4] X. Huang, Y. Lai, Z. H. Hang, H. Zheng, and C. T. Chan, Dirac cones induced by accidental degeneracy in photonic crystals and zero-refractive-index materials, *Nat. Mater.* **10**, 582 (2011).
 - [5] P. Moitra, Y. Yang, Z. Anderson, I. I. Kravchenko, D. P. Briggs, and J. Valentine, Realization of an all-dielectric zero-index optical metamaterial, *Nat. Photonics* **7**, 791 (2013).
 - [6] A. Figotin and I. Vitebskiy, Frozen light in photonic crystals with degenerate band edge, *Phys. Rev. E* **74**, 066613 (2006).
 - [7] M. A. K. Othman, F. Yazdi, A. Figotin, and F. Capolino, Giant gain enhancement in photonic crystals with a degenerate band edge, *Phys. Rev. B* **93**, 024301 (2016).
 - [8] L. Xu, H.-X. Wang, Y.-D. Xu, H.-Y. Chen, and J.-H. Jiang, Accidental degeneracy in photonic bands and topological phase transitions in two-dimensional core-shell dielectric photonic crystals, *Opt. Express* **24**, 18059 (2016).
 - [9] B. Zhen, C. W. Hsu, Y. Igarashi, L. Lu, I. Kaminer, A. Pick, S.-L. Chua, J. D. Joannopoulos, and M. Soljačić, Spawning rings of exceptional points out of Dirac cones, *Nature* **525**, 354 (2015).
 - [10] A. Cerjan, M. Xiao, L. Yuan, and S. Fan, Effects of non-Hermitian perturbations on Weyl Hamiltonians with arbitrary topological charges, *Phys. Rev. B* **97**, 075128 (2018).
 - [11] M. J. Klein, On a degeneracy theorem of Kramers, *Am. J. Phys.* **20**, 65 (1952).
 - [12] X. Zhou, Z.-K. Lin, W. Lu, Y. Lai, B. Hou, and J.-H. Jiang, Twisted quadrupole topological photonic crystals, *Laser Photonics Rev.* **14**, 2000010 (2020).
 - [13] M. Dresselhaus, G. Dresselhaus, and A. Jorio, *Group Theory: Application to the Physics of Condensed Matter* (Springer-Verlag Berlin, 2008), 1st ed.
 - [14] A. Silva, F. Monticone, G. Castaldi, V. Galdi, A. Alù, and N. Engheta, Performing mathematical operations with metamaterials, *Science* **343**, 160 (2014).
 - [15] H. Kwon, D. Sounas, A. Cordaro, A. Polman, and A. Alù, Nonlocal metasurfaces for optical signal processing, *Phys. Rev. Lett.* **121**, 173004 (2018).
 - [16] A. C. Overvig, S. C. Malek, and N. Yu, Multifunctional nonlocal metasurfaces, *Phys. Rev. Lett.* **125**, 017402 (2020).
 - [17] O. Y. Long, C. Guo, H. Wang, and S. Fan, Isotropic topological second-order spatial differentiator operating in transmission mode, *Opt. Lett.* **46**, 3247 (2021).

- [18] J.-H. Song, J. van de Groep, S. J. Kim, and M. L. Brongersma, Non-local metasurfaces for spectrally decoupled wavefront manipulation and eye tracking, *Nat. Nanotechnol.* **16**, 1224 (2021).
- [19] M. Lawrence, D. R. Barton, J. Dixon, J.-H. Song, J. van de Groep, M. L. Brongersma, and J. A. Dionne, High quality factor phase gradient metasurfaces, *Nat. Nanotechnol.* **15**, 956 (2020).
- [20] A. H. Dorrah and F. Capasso, Tunable structured light with flat optics, *Science* **376**, eabi6860 (2022).
- [21] T. Zhu, C. Guo, J. Huang, H. Wang, M. Orenstein, Z. Ruan, and S. Fan, Topological optical differentiator, *Nat. Commun.* **12**, 680 (2021).
- [22] T. Badloe, S. Lee, and J. Rho, Computation at the speed of light: Metamaterials for all-optical calculations and neural networks, *Adv. Photonics* **4**, 064002 (2022).
- [23] S. Fan and J. D. Joannopoulos, Analysis of guided resonances in photonic crystal slabs, *Phys. Rev. B* **65**, 235112 (2002).
- [24] W. Suh, M. F. Yanik, O. Solgaard, and S. Fan, Displacement-sensitive photonic crystal structures based on guided resonance in photonic crystal slabs, *Appl. Phys. Lett.* **82**, 1999 (2003).
- [25] W. Zhou, D. Zhao, Y.-C. Shuai, H. Yang, S. Chuwongin, A. Chadha, J.-H. Seo, K. X. Wang, V. Liu, Z. Ma, and S. Fan, Progress in 2D photonic crystal Fano resonance photonics, *Prog. Quantum Electron.* **38**, 1 (2014).
- [26] C. Guo, M. Xiao, M. Minkov, Y. Shi, and S. Fan, Photonic crystal slab laplace operator for image differentiation, *Optica* **5**, 251 (2018).
- [27] Y. Zhou, H. Zheng, I. I. Kravchenko, and J. Valentine, Flat optics for image differentiation, *Nat. Photonics* **14**, 316 (2020).
- [28] H. Wang, C. Guo, Z. Zhao, and S. Fan, Compact incoherent image differentiation with nanophotonic structures, *ACS Photonics* **7**, 338 (2020).
- [29] O. Y. Long, C. Guo, W. Jin, and S. Fan, Polarization-independent isotropic nonlocal metasurfaces with wavelength-controlled functionality, *Phys. Rev. Appl.* **17**, 024029 (2022).
- [30] D. A. Bykov, L. L. Doskolovich, A. A. Morozov, V. V. Podlipnov, E. A. Bezus, P. Verma, and V. A. Soifer, First-order optical spatial differentiator based on a guided-mode resonant grating, *Opt. Express* **26**, 10997 (2018).
- [31] C. Guo, H. Wang, and S. Fan, Squeeze free space with nonlocal flat optics, *Optica* **7**, 1133 (2020).
- [32] H. Kwon, A. Cordaro, D. Sounas, A. Polman, and A. Alù, Dual-polarization analog 2D image processing with nonlocal metasurfaces, *ACS Photonics* **7**, 1799 (2020).
- [33] J. D. Joannopoulos, S. G. Johnson, J. N. Winn, and R. D. Meade, *Photonic Crystals: Molding the Flow of Light* (Princeton University Press, Princeton, NJ, 2008).
- [34] H. Tang, C. DeVault, S. A. Camayd-Muñoz, Y. Liu, D. Jia, F. Du, O. Mello, D. I. Vulis, Y. Li, and E. Mazur, Low-loss zero-index materials, *Nano Lett.* **21**, 914 (2021).
- [35] T. Ochiai and K. Sakoda, Dispersion relation and optical transmittance of a hexagonal photonic crystal slab, *Phys. Rev. B* **63**, 125107 (2001).
- [36] See Supplemental Material at <http://link.aps.org/supplemental/10.1103/PhysRevApplied.20.L051001> for derivations of \mathbf{b} vector normalization and effective Hamiltonian.
- [37] W. Jin, W. Li, M. Orenstein, and S. Fan, Inverse design of lightweight broadband reflector for relativistic lightsail propulsion, *ACS Photonics* **7**, 2350 (2020).
- [38] J. Roe, *Winding Around: The Winding Number in Topology, Geometry, and Analysis* (American Mathematical Society, Providence, RI, 2015).
- [39] M. Minkov, I. A. D. Williamson, L. C. Andreani, D. Gerace, B. Lou, A. Y. Song, T. W. Hughes, and S. Fan, Inverse design of photonic crystals through automatic differentiation, *ACS Photonics* **7**, 1729 (2020).
- [40] L. C. Andreani and D. Gerace, Photonic-crystal slabs with a triangular lattice of triangular holes investigated using a guided-mode expansion method, *Phys. Rev. B* **73**, 235114 (2006).
- [41] R. C. Gonzalez and R. E. Woods, *Digital Image Processing* (Prentice-Hall, Upper Saddle River, New Jersey, USA, 2006), 3rd ed.
- [42] D. Marr and E. Hildreth, Theory of edge detection, *Proc. R. Soc. Lond. B Biol. Sci.* **207**, 187 (1980).
- [43] C. Guo, M. Xiao, M. Minkov, Y. Shi, and S. Fan, Isotropic wavevector domain image filters by a photonic crystal slab device, *J. Opt. Soc. Am. A* **35**, 1685 (2018).
- [44] E. Hecht, *Optics* (Pearson Education, Harlow, 2017), 5th ed., p. 187.